



A Fractal-designed stretchable and transparent microsupercapacitor as a Skin-attachable energy storage device



Junyeong Yun^a, Hanchan Lee^a, Changhoon Song^a, Yu Ra Jeong^a, Jin Woo Park^b, Jin Ho Lee^c, Dong Sik Kim^a, Kayeon Keum^a, Min Su Kim^c, Sang Woo Jin^c, Yong Hui Lee^a, Jung Wook Kim^a, Goangseup Zi^b, Jeong Sook Ha^{a,c,*}

^a Department of Chemical and Biological Engineering, Korea University, Seoul, 02841, Republic of Korea

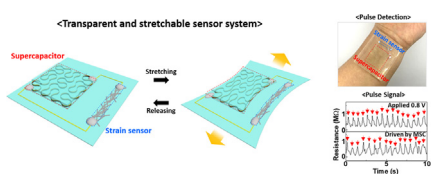
^b Department of Civil, Environmental and Architectural Engineering, Korea University, Seoul, 02841, Republic of Korea

^c KU-KIST Graduate School of Converging Science and Technology, Korea University, Seoul, 02841, Republic of Korea

HIGHLIGHTS

- We report a fractal-designed transparent and stretchable microsupercapacitor (MSC).
- The fabricated MSC exhibits transparency of 79% with a capacitance of 12.6 mF cm^{-2} .
- The MSC maintains electrochemical performance after 2,000 stretching cycles by 30%.
- The strain sensor (SS) can be driven by the integrated MSC.
- The SS powered by the MSC detects wrist bending and arterial pulses.

GRAPHICAL ABSTRACT



ARTICLE INFO

Keywords:
Transparent
Stretchable
Microsupercapacitor
Fractal design
Skin-attachable

ABSTRACT

We report on the fabrication of a fractal-designed transparent and stretchable (TS) microsupercapacitor (MSC) as a skin-attachable energy storage device for driving an integrated strain sensor (SS). The MSC is designed to have a fractal structure with long and narrow patterns to ensure high transparency and stretchability. $\text{MnO}_2/\text{Carbon nanotubes (CNTs)}$ and 1-butyl-3-methylimidazolium bis(trifluoromethylsulfonyl)imide/poly(methyl methacrylate) ([BMIM][TFSI]/PMMA) are used as electrodes and a stretchable electrolyte for the MSC, respectively. The fabricated MSC exhibits high transparency of 79% and an areal capacitance of 12.6 mF cm^{-2} at a current density of 5 mA cm^{-2} . The TS MSC shows excellent mechanical stability in that it can maintain stable electrochemical performance even after 2000 repeated stretching cycles up to 30%. The TS SS is facilely prepared via spray coating of Ag nanowires (NWs) and subsequent curing of PDMS, where the transparency and the electrical resistance are controlled by adjusting the deposited volume of Ag NWs. Wrist bending and a wrist pulse are detected by the SS driven with the stored energy of the MSC. This work demonstrates the possible application of our TS MSC to future skin-attachable electronics as an integrated energy storage device.

1. Introduction

In accordance with the recent increasing interest in and demand for

electronic devices that can be attached to or carried on the human body, extensive studies on small, integrated energy harvesting and storage devices have been performed.^[1–4] In particular, body-

* Corresponding author at: Department of Chemical and Biological Engineering, Korea University, Seoul, 02841, Republic of Korea.
E-mail address: jeongsha@korea.ac.kr (J.S. Ha).

attachable devices should not experience degradation of their performance even under mechanical distortion such as stretching or bending due to body movements, and they are recommended to have transparency considering their long-term wear, especially for the aesthetics. [4–6] In addition, the importance of transparent wearable devices is also emphasized for improving the security of civilian and military applications. [7]

Recently, there has been a growing interest in low cost, high efficiency, high stability, eco-friendly, and reusable energy storage devices. [8–12] Among the various energy storage devices, supercapacitors are expected to be one of the next-generation energy storage devices because of their long cycle life, fast charge and discharge rates, and high power density. [13,14] Supercapacitors are classified into electrical double-layer capacitors (EDLCs) and pseudocapacitors depending on their energy storage mechanism. [15,16] An EDLC uses carbon-based materials, such as carbon nanotubes (CNTs) and graphene, as electrodes, which store energy by electrostatically accumulating charges on the interfaces of the electrodes and electrolytes. [17,18] A pseudocapacitor accumulates electric charges via oxidation/reduction reactions by electrolytic ions of electrode materials such as transition metal oxides and conductive polymers. [19,20]

To implement a high-performance stretchable supercapacitor, the proper materials for efficient electrodes and stretchable structures must be cautiously selected. Stretchable supercapacitors have been mainly fabricated in two ways: First, stretchable structures can be introduced such as wavy structure, kirigami-inspired structure, and pre-strained buckled structure for electrode materials with low elasticity; however, executing this process is very complicated, and ensuring sufficient flexibility is difficult considering the high costs. [21–23] The other approach is to use low-elastic electrode materials with deformable substrates such as fabric, elastomer substrate, and elastic fiber. [24–26] However, the supercapacitors fabricated via the second method exhibit rather poor performance due to the use of a substrate with low conductivity and the high density of the electrode materials. Therefore, a novel strategy to manufacture electrodes with high stretchability, as well as high electrochemical performance, is required. [27]

Indium-doped tin oxide (ITO) is one of the most widely used electrode materials, with high transparency and conductivity. [28] However, ITO has been limited in its application to deformable devices due to its low durability. [29] To obtain flexibility after overcoming such a demerit, various materials, including ultrafine thin films, carbon-based materials, conductive polymers, and metal nanowires with net structures, have been proposed. [30] Transparency is realized for most supercapacitors via coating and patterning of the aforementioned materials on transparent substrates. However, a randomly dispersed electrode network increases the path of electrons and ions during the charge/discharge process and simultaneously delays the flow of electrons. [31] In addition, the transparency of electrodes is inversely proportional to the thickness of the electrode, while the capacitance is directly proportional to the thickness. [32] Therefore, simultaneously obtaining high transparency and high capacitance is not easy.

The fractal design or self-similar concept reported by Fan et al. [33] gives high stability for stretchable electronic devices. Electronic devices based on the fractal concept can have a great advantage of utilizing all the limited space by controlling the fractal order, thereby improving the stretchability. [34] It is also possible to get high transparency by controlling the opening ratio of the fractal designed substrate. Thus, the application of such a fractal design combined with the use of transparent and conducting materials in fabricating a supercapacitor can be an alternative route to the previously reported methods for the stretchable and transparent energy storage devices.

A strain sensor is a device that responds to mechanical deformation by exhibiting changes in electrical properties such as resistance or capacitance. Conventional strain sensors can be facilely fabricated but suffer from low stretchability and sensitivity. [35,36] Especially in the fields of biomechanics and physiology, a highly sensitive strain sensor

with a wide range of strain acceptance is required. [37–39] Carbon-based materials, such as graphenes and CNTs, have been actively used in fabricating strain sensors. [40–43] However, the low stretchability of graphene-based strain sensors and the low sensitivity of CNT-based strain sensors limit their extensive application. [44–47] Silver nanowires (Ag NWs), with excellent electrical conductivity and high transparency, have been studied in various fields, including for use in transparent and flexible devices, solar cells, film heaters, etc. [48–50] However, the low adhesion between Ag NWs and deformable polymeric substrates and the poor contact between adjacent Ag NWs in the repetitive stretching/releasing process have hindered more diverse applications of Ag NW-based sensors.

Even though there have been various reports on the development of high-performance stretchable sensors for detecting environmental and bio-signals, long-wire connections between the sensors and external power supplies limited their wide applications including body-attachable devices. [51–53] Therefore, it is necessary to establish the integration technology of the energy storage devices and the sensors on a single deformable substrate.

In this paper, we propose a novel strategy to fabricate a transparent and stretchable (TS) as well as high electrochemical performance microsupercapacitor (MSC) as a skin-attachable energy storage device. A fractal-designed TS MSC was fabricated using planar MnO₂/CNT electrodes and the TS ionic electrolyte of [BMIM][TFSI]/PMMA. The fabricated TS MSC maintained stable electrochemical performance even under 2000 repeated biaxial stretching cycles up to 30%. In order to detect the biosignals, a strain sensor (SS) was facilely fabricated by a simple spray coating of Ag NWs on PDMS and its subsequent curing. The transparency and resistance of the SS could be adjusted by controlling the deposited amount of Ag NWs. After integrating the MSC and SS on a single stretchable substrate, the SS could be driven by the MSC to detect a wrist pulse as well as wrist bending. This work suggests a possible route to fabricate a TS MSC as an integrated energy storage device for driving the skin-attachable biosensor.

2. Experimental section

2.1. Synthesis of the stretchable electrolyte [BMIM][TFSI]/PMMA

The stretchable electrolyte was synthesized via modification of a previously reported work. [54] First, 500 mg of poly(methyl methacrylate) (PMMA, MW:99000 g mol⁻¹, Sigma Aldrich) was added to 20 ml of acetone (for HPLC, ≥99.9%, Sigma Aldrich) and stirred until clear. After adding 1 g of 1-butyl-3-methylimidazolium bis(trifluoromethylsulfonyl)imide ([BMIM][TFSI], Sigma Aldrich) to the solution, it was stirred at 400 rpm for 6 hr. PMMA has a very high solubility in acetone, and this solution also mixes well with [BMIM][TFSI].

2.2. Fabrication of the transparent and stretchable fractal-designed MnO₂/CNT microsupercapacitor

A silica substrate (SiO₂, dry type 1000 Å, P type, Inexus Inc.) was rinsed with acetone and DI water and simply dried with a N₂ gas gun. Then, polyimide solution (PI, DFCPI-101, Dongbaek Fine-Chem) was spin coated on the SiO₂ substrate (500 rpm for 10 s and 4000 rpm for 1 min) and cured on a hot plate at 260 °C for 4 hr. Cr and Au electrodes were deposited on a PI/SiO₂ substrate via an e-beam evaporation process (KVE-T4605, Korea Vacuum Tech). Then, the Au/PI surface was modified with self-assembled monolayer treatment of (3-aminopropyl) triethoxysilane (APTES) to increase the adhesion between the spray-coated CNTs and substrate. The prepared Au/PI was immersed in 10 mM APTES solution for 12 hr, modifying the surface to be hydrophilic due to the amine functional groups on the Au/PI substrate. Multiwalled carbon nanotubes functionalized with carboxylic acid groups (CNT-COOH) were synthesized through an acid treatment

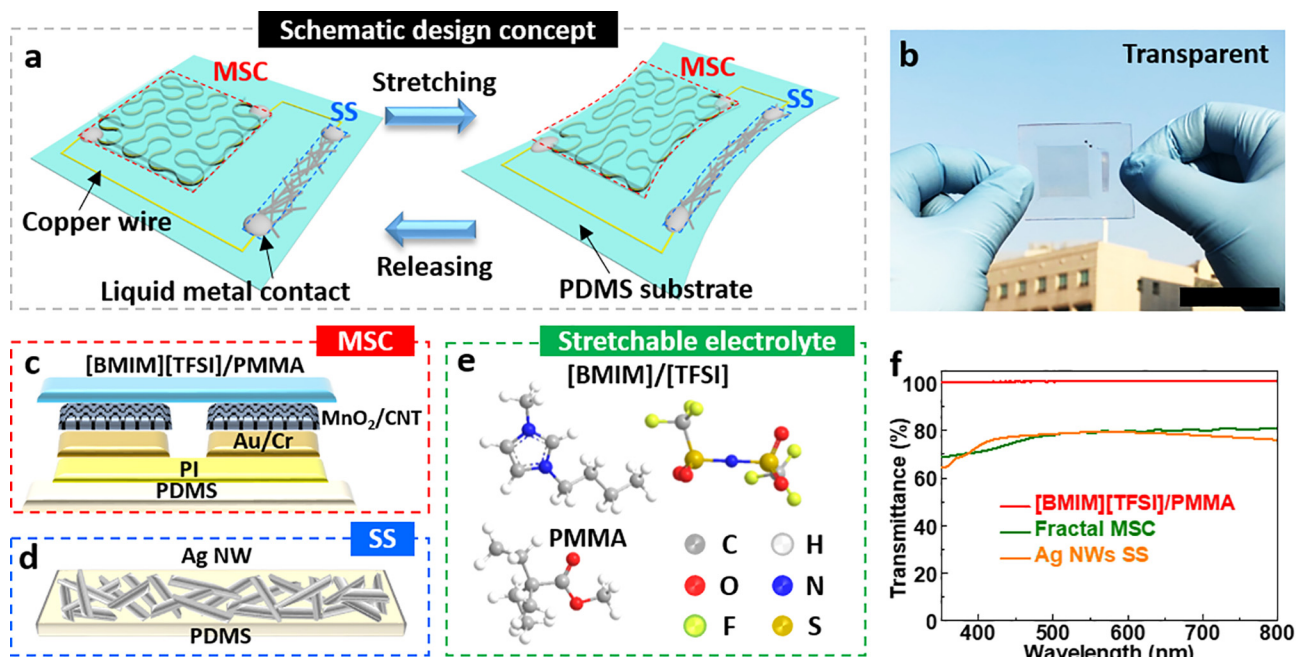


Fig. 1. (a) Schematic illustration and (b) photograph of a transparent and stretchable microsupercapacitor (MSC) integrated with a Ag NW strain sensor (SS). The scale bar corresponds to 5 cm. Cross-sectional view of (c) the MSC and (d) SS. (e) Molecular structures of the components of the stretchable ionic electrolyte [BMIM][TFSI]/PMMA. (f) Transmittance spectrum of (red) [BMIM][TFSI]/PMMA, (green) the fractal MSC, and (orange) the Ag NW SS. (For interpretation of the references to colour in this figure legend, the reader is referred to the web version of this article.)

process. The acid treatment was as follows: 500 mg of CNTs (≥ 99 wt%, $\leq 13\text{--}18$ nm OD, MW 30–141, Nanointegris) was mixed with 30 ml of sulfuric acid (H_2SO_4 , 99.999%, Sigma Aldrich) and 10 ml of nitric acid (HNO_3 , 70%, ACS reagent, Sigma Aldrich). Then, this CNT acid solution was refluxed at 70 °C for 4 hr. After the refluxing process, the CNT acid solution was diluted with 1 l of deionized water (DI water) and cooled to room temperature. Then, this solution was vacuum filtered with a mixed cellulose filter (0.2 µm, Advantec MFS, Inc.). To remove residual acid from the filtered CNTs, the CNTs were dispersed in DI water and then dialyzed by a dialysis tubing cellulose membrane (MW = 12000 g mol⁻¹, Sigma Aldrich) in a DI water bath with stirring. After dialysis, the dispersed CNTs were vacuum filtered and dried at room temperature. The dried CNTs were dispersed in DI water (1 g/L) for the spray deposition process. A total of 10 ml of this CNT dispersion solution was spray coated on the APTES-treated Au/PI substrate. Then, the CNT/Au substrate was immersed in a mixture of 500 ml of a 0.1 M KMnO₄ (≥ 99 %, ACS reagent, Sigma Aldrich) solution and 10 ml of methanol (for HPLC, ≥ 99 %, Sigma Aldrich) for deposition of MnO₂ for 16 hr. Finally, we obtained a MnO₂/CNT/Au/PI film. Then, this film was patterned with a fractal design via an etching process based on photolithography. First, the top CNT film was etched with a fractal pattern via a reactive ion etching process (RIE, 100 W, O₂, 20 sccm, 130 mTorr, 30 s). Then, the Au and Cr film were etched via a simple immersion process; wet etching was performed with a commercial Au etchant (Transene, Gold Etch-Type TFA) and a Cr etchant (Aldrich, Chromium Etchant). The fractal-designed MnO₂/CNT/Au/PI was transferred onto a PDMS elastomer substrate (polydimethylsiloxane, PDMS, base:curing agent = 30:1) using commercial water-soluble tape (WST, 5414 1 × 36, 3 M company). After the MnO₂/CNT/Au/PI transfer process, the WST was easily removed by DI water. A total of 50 µl of the prepared electrolyte [BMIM][TFSI]/PMMA was dropped on the fractal-designed MnO₂/CNTs, then dried at room temperature for a day and vacuum dried for 12 hr. Finally, a fractal-designed MnO₂/CNT microsupercapacitor (MSC) with the stretchable electrolyte [BMIM][TFSI]/PMMA was fabricated.

2.3. Fabrication of the transparent Ag NW strain sensor

The Ag NW strain sensor was fabricated by a simple fabrication process. First, the commercial Ag NW dispersion solution (1 wt% DI water dispersion, Dittotechnology) was spray-coated onto commercial polytetrafluoroethylene film (PTFE, Sigma Aldrich). Then, uncured PDMS (base:curing agent = 30:1, weight ratio) was poured on this film and cured at 60 °C for 24 hr. After the removal of the PTFE film from the cured PDMS substrate, the Ag NWs were left on the PDMS surface.

2.4. Integration of the transparent and stretchable MSC with the strain sensor

The fabricated MSC and strain sensor were placed on the front surface of the device facing the bottom of a petri dish. Then, uncured PDMS was poured onto the device and cured at 60 °C for 24 hr. Finally, a transparent and stretchable MSC with a strain sensor was fabricated, and each device was connected via externally connected Cu wires at liquid metal contacts (Galinstan, Gallium Source Company).

2.5. Characterization

Scanning electron microscope (SEM, Quanta 250 FEG, FEI, Thermo Fisher Scientific), FT-IR and Raman spectroscopy (LabRam ARAMIS IR2, HORIBA JOBIN YVON), XPS (X-TOOL, ULVAC-PHI) and XRD (SmartLab, Rigaku) were used to investigate the surface morphology and chemical composition of the synthesized electrodes and electrolyte. The electrochemical performance was evaluated by measuring CV curves, galvanostatic charge/discharge curves, and the electrochemical impedance (Ivium Technologies, Compact Stat).

3. Result and discussion

In Fig. 1, the schematic concept (Fig. 1a) and a photograph (Fig. 1b) of the TS MSC integrated with the Ag NW SS are shown. The detailed fabrication processes are explained in Fig. S1 and the Experimental

section. To achieve a TS integrated system consisting of an MSC and an SS, novel strategies were adopted. As shown in the cross-sectional scheme of Fig. 1c, our MSC consists of MnO_2/CNTs as electrodes and [BMIM][TFSI]/PMMA as a stretchable electrolyte on a PI/PDMS substrate. The MSC has two planar electrodes on the substrate with a symmetric structure, and the MSC is designed based on a previously reported fractal structure. [33] This fractal structure has a structural self-similarity, with geometrical pieces similar to the whole when subdivided into small parts, as shown in Fig. S2. The fractal design can better support reinforced elastic deformations and biaxial, radial and other deformation modes for the selected dimensions compared to periodic serpentine-shaped networks. Therefore, we adopted this fractal design for the fabrication of our stretchable MSC. In addition, we adjusted the width of the entire fractal-designed electrodes and the interspace between electrodes to ensure transparency, as shown in Fig. S3, thereby achieving an opening ratio of 92.1%. The detailed opening ratio calculation is given in Fig. S4. Furthermore, we were able to achieve better transparency and stretchability of the MSC by applying the TS ionic liquid-based electrolyte [BMIM][TFSI]/PMMA to our MSC. [54] The molecular structures of individual components of the [BMIM][TFSI]/PMMA electrolyte are shown in Fig. 1e. Since the electrolyte was in a solid-state, there appeared no leakage problem. In addition, owing to the low vapor pressure of ionic liquids such as [BMIM][TFSI] at room temperature, the solid electrolyte prepared by mixing with PMMA is expected not to result in serious risk of evaporation. [55,56]

A transparent SS based on Ag NW network for detecting body movement and pulses was facilely fabricated via spray coating of a Ag NW solution and subsequent curing of PDMS. Fig. 1d shows a cross-sectional scheme of the Ag NW-based SS. The transparency and resistance of the SS could be optimized by adjusting the amount of Ag NW solution. In particular, a strategy to increase the initial resistance of the SS was adopted for long-term operation using the finite energy stored in the integrated MSC.

By integrating the fabricated MSC and SS onto a single PDMS substrate, a TS sensor system could be obtained. The transmittances of the electrolyte, fractal-designed MSC, and SS were measured to be 99%, 79%, and 79%, respectively, in the visible range of 550 nm, as shown in Fig. 1f. This result signifies the high transparency of our fabricated devices.

In Fig. 2, the structural and chemical properties of the electrode and electrolyte materials are given. A scanning electron microscopy (SEM) image and a magnified SEM image of the fractal-designed electrodes are shown in Fig. 2a and 2b, respectively. Fractal-design patterned electrodes with an interspace of 3 μm between electrodes are clearly observed. Energy dispersive spectroscopy (EDS) measurements were performed to investigate the spatial distribution of the MnO_2/CNT component elements on the fractal-designed electrodes, as shown in Fig. 2c. Au, C, Mn, and O are observed to be uniformly distributed over the entire fractal-designed electrodes. Moreover, no elements exist in the interspace between electrodes, signifying that our fabrication processes based on photolithography and etching functioned as desired. A uniform distribution of electrode materials is important for efficient ion transfer between the electrode and electrolyte to achieve high electrochemical performance. Fig. 2d shows an SEM image of the CNT network film surface, showing a porous structure with pore diameters of 10–100 nm. Fig. 2e shows an SEM image of the MnO_2/CNT network film, which also shows a porous structure with pore diameters of 10–20 nm. Such a nanoscale porous structure ensures a large specific area and is expected to result in high electrochemical performance. SEM images taken from the MnO_2/CNTs film with the increase of MnO_2 growth time are also shown in Fig. S5. As the growth time increases, the amount of MnO_2 grown on the CNTs gradually increases and after 24 h, the porous structure of the electrode surface is dramatically reduced. Fig. 2f shows the Fourier transform infrared (FT-IR) spectra of CNTs (black) and MnO_2/CNTs (red). In the FT-IR spectrum of the CNTs, C=O stretching of the carboxyl group of the functionalized CNTs is observed

at 1686 cm^{-1} . [57] In the FT-IR spectrum of MnO_2/CNTs , a peak is observed at approximately 3255 cm^{-1} due to –OH stretching vibration. [58] The absorption peaks at 1636 cm^{-1} and 1375 cm^{-1} correspond to O–H bending vibrations combined with Mn atoms. [59] In Fig. 2g, the Mn 2p X-ray photoelectron spectroscopy (XPS) results show the $\text{Mn}2\text{p}_{3/2}$ peak at 641.9 eV and the $\text{Mn}2\text{p}_{1/2}$ peak at 653.5 eV. The difference in energy between the two peaks is 11.6 eV, demonstrating the existence of MnO_2 . [60] In Fig. 2h, the O1s spectrum shows binding energies related to anhydrous MnO_2 (Mn-O-Mn) at 529.4 eV and hydrated MnO_2 (Mn-O-H) at 531.7 eV. [61] We synthesized the electrode material for the MSC via bath deposition of MnO_2 over a CNT network. As shown in Fig. S6, the areal capacitance was measured for various deposition times of MnO_2 up to 16 hr. The capacitance was 0.46 mF cm^{-2} when CNTs were used without MnO_2 , and it continuously increased with increasing MnO_2 deposition time, resulting in 12.6 mF cm^{-2} after growth for 16 hr. The growth time was limited to 16 hr due to the destructive influence on the subsequent fractal electrode fabrication process beyond 16 hr of growth. As described in the experimental section, the fractal-designed electrode can be fabricated via reactive ion etching (RIE) after bath deposition of MnO_2 . As shown in Fig. S7, the RIE process could not be performed on the electrodes with MnO_2 deposited for longer than 16 hr, which also made subsequent processing impossible. This limitation occurred because over-deposited MnO_2 prevents etching of CNTs in the RIE process. [BMIM][TFSI]/PMMA was used as a TS electrolyte. Fig. 2i shows FT-IR spectra for [BMIM][TFSI]/PMMA, [BMIM][TFSI], and PMMA. The FT-IR spectrum of PMMA presents two noteworthy peaks. The broad peak between 1081 cm^{-1} and 1219 cm^{-1} is due to ester bond (C–O) stretching vibration, and the sharp peak at 1720 cm^{-1} corresponds to ester carbonyl group stretching vibration. [62] The FT-IR spectrum of [BMIM][TFSI] exhibits several peaks at $\sim 783 \text{ cm}^{-1}$ indicating the existence of C–S and S–N stretching, an in-plane C–H bending peak of the imidazolium ring at 839 cm^{-1} , a S–N–S stretching peak at 1052 cm^{-1} , a N–H stretching peak at 1213 cm^{-1} , and a SO₂ asymmetric stretching peak of the counter anion of [TFSI]⁻ at 1344 cm^{-1} . [63] The FT-IR spectrum of [BMIM][TFSI]/PMMA exhibits all the peaks observed for [BMIM][TFSI] and PMMA, indicating the formation of a well-mixed electrolyte. We can synthesize a stable electrolyte for the TS MSC by controlling the weight ratio of [BMIM][TFSI] to PMMA. Fig. S8 shows the change in capacitance with the variation of the weight ratio of [BMIM][TFSI] to PMMA between 0.2 and 2.0 at an interval of 0.2. At a weight ratio of 0.2, a very low capacitance of 0.089 mF cm^{-2} is obtained, while the capacitance significantly increases up to 12.6 mF cm^{-2} at a weight ratio of 2.0. Above the weight ratio of 2.0, complete mixing of [BMIM][TFSI] with PMMA cannot be achieved since the excess [BMIM][TFSI] compared to PMMA induces leakage. Up to the weight ratio of 0.8, the electrolyte is hard to deform; in contrast, it can be freely deformed while exhibiting high transparency above this value up to the weight ratio of 2.0. Therefore, we optimized the weight ratio of the electrolyte at 2.0, where the highest transparency and stretchability as well as the highest capacitance of our MSC could be obtained.

In Fig. 3, the electrochemical properties of the TS MSC are compared for electrodes of CNTs and MnO_2/CNTs with the same TS electrolyte of [BMIM][TFSI]/PMMA. The cyclic voltammetry (CV) curves of the two TS MSCs, measured at a scan rate of 10 mV s^{-1} , present nearly rectangular shapes in Fig. 3a, indicating the ideal behavior of the electrode materials and current-voltage changes that occur at the same time with rapid ion transfer. [64] The capacitance increases dramatically with deposition of MnO_2 onto the CNTs. Fig. 3b shows the galvanostatic charge/discharge curves of the two different electrode-based TS MSCs at a current density of 10 $\mu\text{A cm}^{-2}$. Both charge/discharge curves exhibit symmetric triangular shapes with straight lines, which appear for ideal supercapacitors. [65] The charge/discharge times for the CNT and MnO_2/CNT TS MSCs were estimated to be 23 s and 460 s, respectively. In this study, we calculated all the electrochemical properties of the MSCs, such as the capacitance, energy density, and power

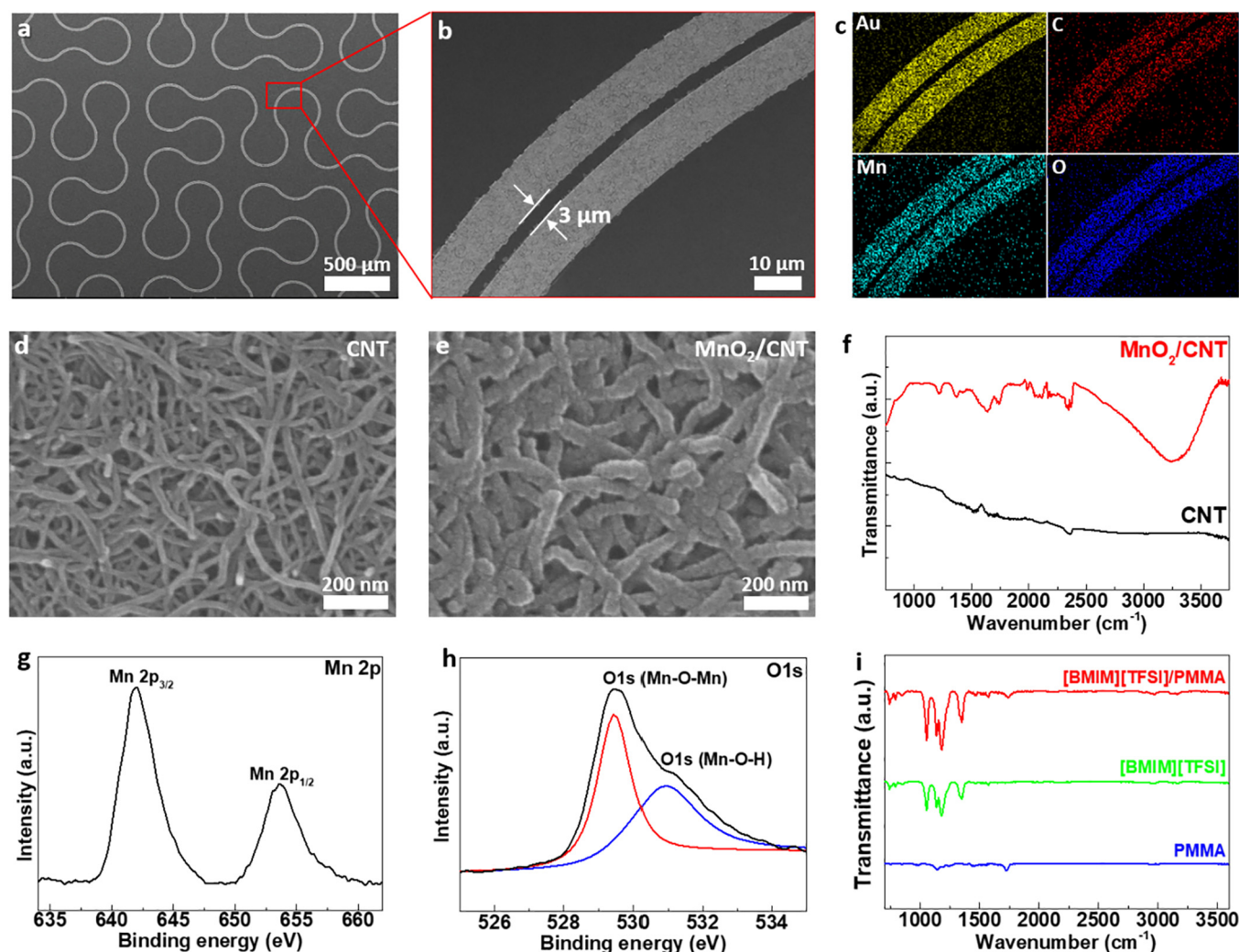


Fig. 2. (a) SEM image and (b) magnified SEM image of fractal-designed electrodes. (c) EDS mapping of the fractal-designed electrodes showing the areal distributions of Au, C, Mn, and O elements. SEM images of (d) CNT and (e) MnO₂/CNT films. (f) FT-IR spectra of CNTs (black) and MnO₂/CNTs (red). XPS spectra of (g) the Mn 2p peaks and (h) the O 1s peaks. (i) FT-IR spectra of [BMIM][TFSI]/PMMA (red), [BMIM][TFSI] (green), and PMMA (blue). (For interpretation of the references to colour in this figure legend, the reader is referred to the web version of this article.)

density, on an area metric. The areal capacitance (C_a , F cm⁻²) was calculated by equation (1):

$$C_a(F\text{cm}^{-2}) = \frac{I(A) \times \Delta t(s)}{\Delta V(V) \times A(\text{cm}^2)} \quad (1)$$

where I, Δt , ΔV , and A are the discharge current density (A), discharge time (s), discharge voltage (V), and electrodes area (cm⁻²), indicating total square area as shown in Fig. S4. Fig. 3c shows the change in the areal capacitance of the CNT and MnO₂/CNT TS MSCs with current density. The capacitances of the CNT and MnO₂/CNT TS MSCs were estimated to be 0.46 mF cm⁻² and 12.59 mF cm⁻² at a current density of 10 $\mu\text{A cm}^{-2}$, 0.43 mF cm⁻² and 9.81 mF cm⁻² at a current density of 100 $\mu\text{A cm}^{-2}$, and 0.32 mF cm⁻² and 7.69 mF cm⁻² at a current density of 500 $\mu\text{A cm}^{-2}$, respectively. In addition, a very small standard deviation of the capacitance, indicated by the error bars, was calculated from 10 different TS MSCs, suggesting the high reproducibility of our TS MSCs. Fig. 3d shows Nyquist impedance plots in the frequency range of 1 MHz to 0.1 Hz. Through this impedance analysis, transfer of charges and ion diffusion characteristics in the TS MSCs with frequency changes can be determined. The virtual region of Z'' (Y-axis) represents the capacitive parameter, and the actual component of Z (X-axis) represents the ohmic parameter. [66] The equivalent series resistance (ESR), indicating charge transfer resistance,

is measurable on the X-axis. [67] The ESR values for the CNT and MnO₂/CNT TS MSCs were estimated to be 141 Ω and 98 Ω , respectively. The MnO₂/CNT TS MSC has a smaller ESR value than the CNT TS MSC, implying that the MnO₂/CNT TS MSC has a smaller charge transfer resistance. Both TS MSCs exhibit semicircular shapes of different sizes in the high-frequency region, indicating the larger contact resistance of the electrolyte with the CNT electrode than with the MnO₂/CNT electrode. [68] This result is quite unexpected but can probably be explained in terms of the chemical processes performed in this work. As described in the experimental section, the fractal-designed supercapacitor was fabricated via photolithography and a subsequent etching process. To realize perfect etching, a much thinner CNT network film compared to that used in our previous work was deposited. [69] As a result, the CNT film electrode might exhibit relatively low conductivity with a low specific surface area at the electrode-electrolyte interface. To solve such problems, we performed chemical bath deposition of MnO₂, which further affected the resultant electrochemical properties of the fabricated supercapacitor. Similar results of improvements in the ion accessibility and transfer efficiency of carbon-based materials via deposition of pseudocapacitive materials were previously reported. [70–72] In addition, the presence of impedance graphs parallel to the Y-axis in the low-frequency region indicates a low ion diffusion resistance within the electrode structure. [73] Fig. 3e

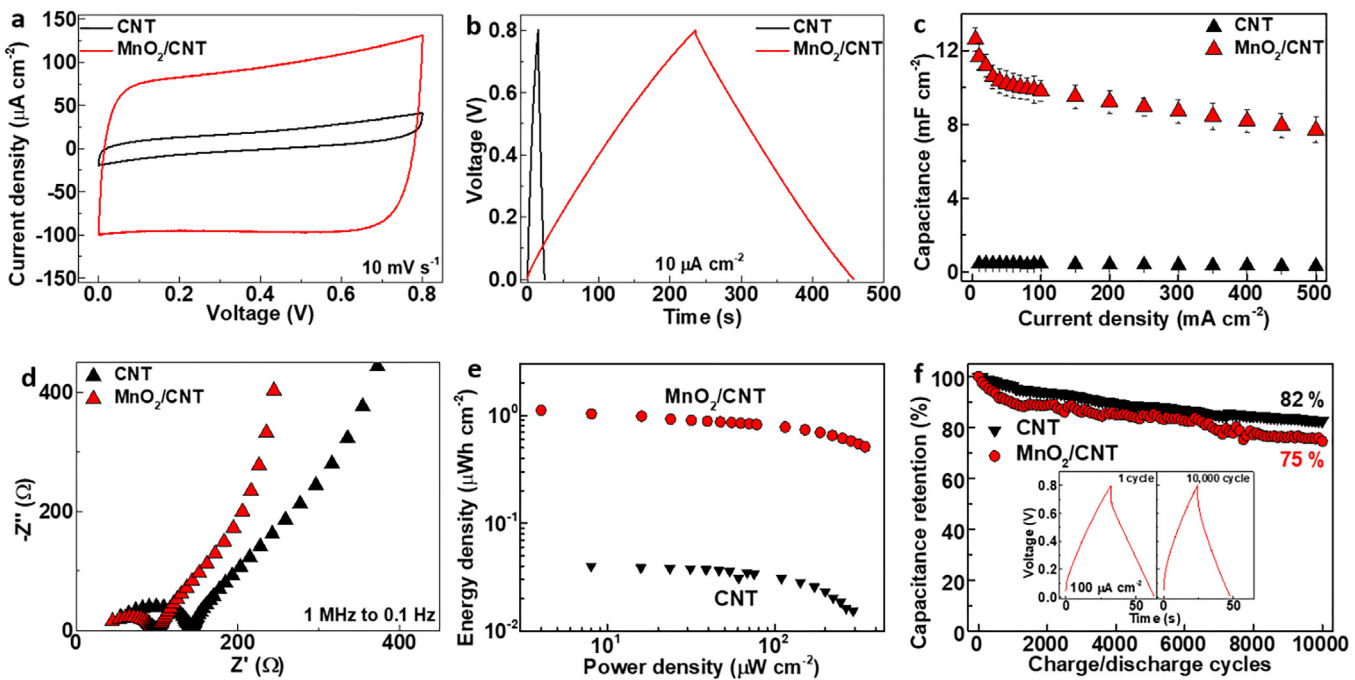


Fig. 3. Electrochemical performance of the MSCs with CNTs (red) and MnO₂/CNTs (black). (a) CV curves at a scan rate of 10 mV s⁻¹. (b) Galvanostatic charge/discharge curves at a scan rate of 10 μA cm⁻². (c) Areal capacitance from 15 different MSCs with error bars. (d) Nyquist impedance plots. (e) Ragone plot. (f) Capacitance retention in the charge/discharge cycles at a scan rate of 100 μA cm⁻². The inset shows the charge/discharge curves for the 1st and 10000th cycles. (For interpretation of the references to colour in this figure legend, the reader is referred to the web version of this article.)

shows Ragone plots of the energy density (E , Wh cm⁻²) versus the power density (P , W cm⁻²). The energy density and power density were calculated by equations (2) and (3):

$$E(\text{Whcm}^{-2}) = \frac{C_a(\text{Fcm}^{-2}) \times \Delta V^2(\text{V})}{7200} \quad (2)$$

$$P(\text{Wcm}^{-2}) = \frac{E(\text{Whcm}^{-2})}{\Delta t(\text{s})} \times 3600 \quad (3)$$

where E , P , C_a , ΔV , and Δt represent the energy density (Wh cm⁻²), power density (W cm⁻²), areal capacitance (F cm⁻²), voltage range (V), and discharge time (s). The maximum energy density of the CNT TS MSC is 0.04 μWh cm⁻² at a power density of 7.94 μW cm⁻², and that of the MnO₂/CNT TS MSC is 1.12 μWh cm⁻² at a power density of 3.99 μW cm⁻². Fig. 3f shows the cycling stability, determined through repeated charge/discharge cycles of the two TS MSCs at a current density of 100 μA cm⁻². The CNT TS MSC and MnO₂/CNT TS MSC maintained 82% and 75% of the initial capacitance, respectively, after 10000 repeated charge/discharge cycles. Through the analysis of the electrochemical properties in Fig. 3, we confirmed that the MnO₂/CNT TS MSC has improved electrochemical characteristics compared to the CNT TS MSC. In addition, the fabricated MnO₂/CNT TS MSC was placed in the air, and the capacitance retention according to the time elapsed was measured, as shown in Fig. S9. When the TS MSC was exposed to air at room temperature, 92% of the initial capacitance was maintained, even after 360 hr. Fig. S10 shows an optical image of the integrated system consisting of the TS MSC and a commercial liquid crystal display (LCD) watch connected via an external copper wire. Once the TS MSC of the integrated system was charged, the LCD could be driven for approximately 5 min. Considering the very small surface coverage of the fractal-designed electrodes, ~8%, our MSC is appealing as a sufficient energy source for electronic devices.

Fig. 4 shows the mechanical stability of the fractal-designed TS MSC in biaxial stretching. Optical images of the hand-held TS MSC before and after biaxial stretching along the directions of the orange arrows are given in Fig. 4a. The applied biaxial strain ($\varepsilon_{\text{biaxial}}$) was calculated

by equation (4):

$$\varepsilon_{\text{biaxial}} = \frac{(l' - l)}{l} \quad (4)$$

where l and l' are the length of the initial and stretched states of the TS MSC, respectively. The strain distribution of the fractal-designed TS MSC was analyzed using the finite element method (FEM). Fig. 4b shows optical images and results of the FEM analysis of the smallest change unit of the fractal-designed TS MSC with increasing biaxial stretching. The top two images were obtained from the TS MSC in stretching states of 0% and 20%. As shown in the images, the fractal-designed TS MSC reliably stretches without any disconnection. The bottom images of Fig. 4b are from the analysis of the strain distribution when the TS MSC was stretched in biaxial directions by 0, 5, 10, 15, 20, 25, and 30%. The results of the FEM analysis in quarter view are shown in Fig. S11. As clearly confirmed, the narrow and long fractal-designed pattern works well without a noticeable problem even when stretched by 30% in biaxial directions, as reported by Fan et al. [33]. Fig. S12 shows an analysis of the strain distribution when the TS MSC was stretched in a uniaxial direction by 0, 5, 10, 15, 20, 25, and 30%. Fig. 4c and 4d show the CV curves and galvanostatic charge/discharge curves measured after biaxially stretching the TS MSC by 0%, 5%, 10%, 20%, 25%, and 30%. No noticeable degradation of the electrochemical performance is observed upon stretching deformation, with a negligible change within 2%. Fig. 4e shows the capacitance retention obtained after repeated stretching of the TS MSC up to 30%. The capacitance retention was calculated from the galvanostatic charge/discharge curves measured at every 50 stretching cycles. The TS MSC maintains 96% of its initial capacitance after 2000 repeated stretching cycles, confirming the mechanical stability of our TS MSC.

To detect biosignals using the energy stored in our TS MSC, a transparent Ag NW-based SS was fabricated via simple spray coating of Ag NW solution onto PDMS and subsequent curing of the PDMS elastomer. As shown in Fig. S13, the transmittance of the SS as a function of the deposited volume of Ag NW solution was investigated. In this work, we used 0.5 ml cm⁻² Ag NWs for the SS with a transparency of 79% at a

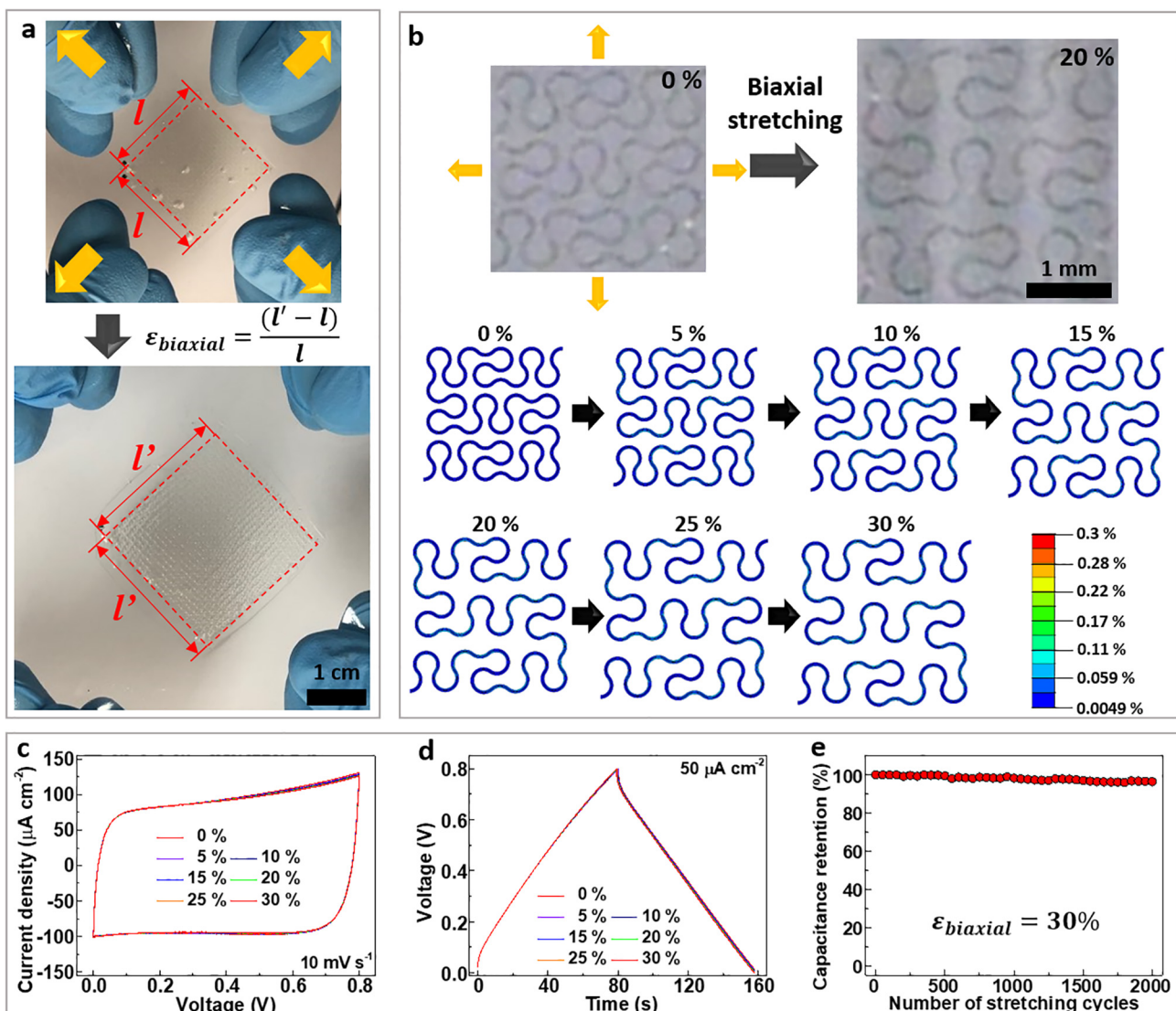


Fig. 4. (a) Schematic definition of the biaxial strain $\epsilon_{biaxial}$. (b) Top-view optical images (top) and FEM analysis of a fractal-designed MSC in various biaxial stretching states. (c) CV curves and (d) charge/discharge curves for various applied biaxial strains. (e) Capacitance retention with repetitive stretching to 30%.

wavelength of 550 nm. An SEM image of the fabricated Ag NW SS before stretching (0%) is shown in Fig. 5a, where the Ag NWs form a porous network structure. Upon stretching by 30%, the Ag NWs are aligned along the stretching direction but still maintain the percolated network, as shown in the inset SEM image. Fig. 5b shows the relative resistance ($\Delta R/R_0$) vs. strain curve with the increase of strain, where the slope exhibits the gauge factor. The gauge factor is defined following the equation (5):

$$\text{Gaugefactor} = \frac{\Delta R/R_0}{\epsilon} \quad (5)$$

where ΔR , R_0 , and ϵ represent the change of resistance upon application of strain, the resistance at a strain of 0%, and the applied strain, respectively. The gauge factor is estimated to be 32.8 at 30%. The inset of Fig. 5b exhibits the current-voltage (I-V) curves obtained from the Ag NW SS for various strains of 0%, 10%, 20%, and 30%. The linear dependence of the current change on the voltage change signifies that the fabricated Ag NW SS is a resistor-type sensor. The sensing mechanism of the Ag NW SS for an applied strain is shown in Fig. S14. As the PDMS is stretched due to the applied strain, the distance between adjacent Ag NWs on the PDMS is increased, thus increasing the resistance. Wrist movements and pulses were measured using the SS

powered by both the integrated MSC and an external power supply after attachment of the whole system onto the wrist skin. Those configurations can be compared in Fig. S15. Fig. 5c shows a photograph of the TS integrated system consisting of the MSC and SS attached to a wrist to detect wrist movements. Tensile strain is applied to the TS integrated system in the direction of the black arrow when the wrist is bent, as shown in the inset photograph. Such movement of the wrist is observed as a current change in Fig. 5d. The top and bottom graphs were measured by applying an external constant voltage of 0.8 V and our integrated MSC to the sensor, respectively. Here, the red and blue arrows represent the wrist motions of bending and straightening, respectively. A current of $\sim 750\text{nA}$ flowed before bending of the wrist, but the current decreased to $\sim 250\text{nA}$ upon bending due to the increase in the resistance. We repeated these wrist bending (B_1, B_2, B_3, B_4 , and B_5)-straightening (F_1, F_2, F_3, F_4 , and F_5) cycles five times at intervals of 4 s, and a constant current change from 750 to 250nA was observed. The same bending (B_6, B_7, B_8, B_9 , and B_{10})-straightening (F_6, F_7, F_8, F_9 , and F_{10}) cycles were also repeated with our integrated system consisting of the MSC and SS. Unlike the case with the use of an external power system, the current flow gradually decreased with time. Such a decrease in current is caused by the limited capacitance of the MSC. However, we confirmed that the sensor can detect the bending and straightening

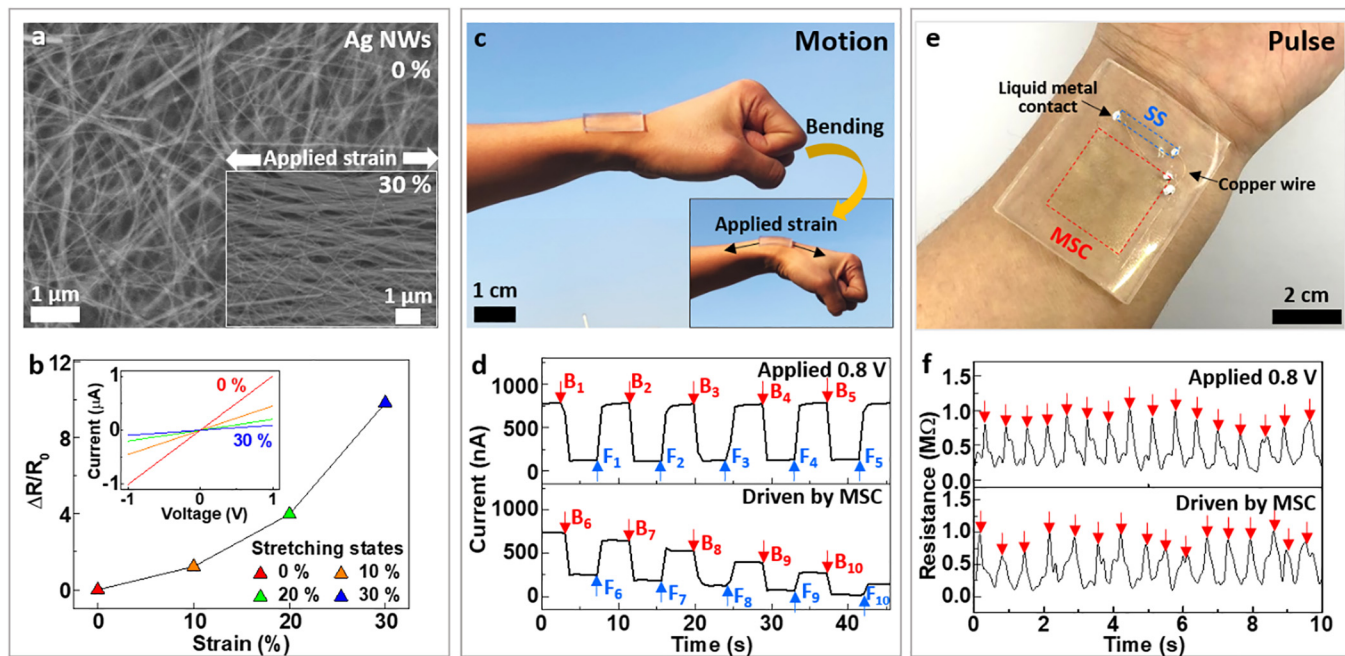


Fig. 5. (a) SEM image of a Ag NW network on PDMS before stretching (0%). The inset is an SEM image under 30% stretching. (b) The relative change in resistance ($\Delta R/R_0$) versus strain curves of the Ag NW strain sensor taken for various stretching states from 0 to 30%. (Inset) I-V curves of the sensor taken with variation of strain from 0 to 30%. (c) Photograph of wrist bending with a skin-attached MSC-SS system. (d) Current change of the Ag NW SS with wrist motion, where red and blue arrows correspond to bending and straightening, respectively. The top and bottom graphs are obtained from the SS driven by an externally applied constant voltage of 0.8 V and by our MSC, respectively. (e) Photograph of the integrated system attached to the skin of the wrist. (f) Resistance change of the Ag NW SS with the wrist pulse. The top and bottom graphs are obtained from the SS driven by an externally applied constant voltage of 0.8 V and by our MSC, respectively. (For interpretation of the references to colour in this figure legend, the reader is referred to the web version of this article.)

of the wrist regardless of the power source. Fig. 5e shows a photograph of our wrist-attached TS integrated system measuring the wrist pulse of a 30-year-old male graduate student. Here, the integrated system was lightly placed on the wrist, and pulse detection was performed. A liquid metal, Galinstan, was deposited on each electrode pad of the MSC and sensor, and these pads were connected through copper wires, as shown in Fig. 1a. Fig. 5f shows the pulse measurement data obtained from the sensor driven by an external power source and the energy stored in the MSC. Both graphs show similar resistance changes, regardless of the power source. Sixteen pulse signals were detected in 10 s at uniform intervals. These results demonstrate that both large strains induced by wrist bending and small ones due to wrist pulses can be detected using the SS driven by the integrated TS MSC.

4. Conclusion

A fractal-designed transparent and stretchable (TS) microsupercapacitor (MSC) was fabricated as a skin-attachable energy storage device for driving a strain sensor (SS) to detect biosignals. The MSC designed with a long and narrow fractal pattern ensured high transparency and stretchability. Bath deposition of MnO₂ over spray-coated carbon nanotubes (CNTs) was used to fabricate the electrodes, and ionic [BMIM][TFSI]/PMMA was used as a TS electrolyte. The fabricated MSC maintained its initial capacitance without significant change even after 2000 repeated stretching cycles up to 30% stretching. A TS SS based on the Ag-nanowire network could detect both wrist bending and a wrist pulse using the stored energy of the integrated MSC, demonstrating the high application potential of our fractal-designed MSC as a future skin-attached TS energy storage device for bioelectronics.

Declaration of Competing Interest

The authors declare that they have no known competing financial

interests or personal relationships that could have appeared to influence the work reported in this paper.

Acknowledgments

This work was supported by a National Research Foundation of Korea, South Korea (NRF) grant funded by the Korean government (MSIP) (Grant No. NRF-2019R1A2B5B03069545). The authors also thank the KU-KIST graduate school program of Korea University.

Appendix A. Supplementary data

Supplementary data to this article can be found online at <https://doi.org/10.1016/j.cej.2020.124076>.

References

- [1] X. Wang, C. Yang, J. Jin, X. Li, Q. Cheng, G. Wang, High-performance stretchable supercapacitors based on intrinsically stretchable acrylate rubber/MWCNTs@conductive polymer composite electrodes, *J. Mater. Chem. A* 6 (2018) 4432–4442.
- [2] Z. Niu, H. Dong, B. Zhu, J. Li, H.H. Hng, W. Zhou, X. Chen, S. Xie, Highly stretchable, integrated supercapacitors based on single-walled carbon nanotube films with continuous reticulate architecture, *Adv. Mater.* 25 (2013) 1058–1064.
- [3] S. Park, H. Kim, M. Vosgueritchian, S. Cheon, H. Kim, J.H. Koo, T.R. Kim, S. Lee, G. Schwartz, H. Chang, Z. Bao, Stretchable energy-harvesting tactile electronic skin capable of differentiating multiple mechanical stimuli modes, *Adv. Mater.* 26 (2014) 7324–7332.
- [4] K.S. Kim, Y. Zhao, H. Jang, S.Y. Lee, J.M. Kim, K.S. Kim, J.-H. Ahn, P. Kim, J.-Y. Choi, B.H. Hong, Large-scale pattern growth of graphene films for stretchable transparent electrodes, *Nature* 457 (2009) 706.
- [5] B.-U. Hwang, J.-H. Lee, T.Q. Trung, E. Roh, D.-I. Kim, S.-W. Kim, N.-E. Lee, Transparent stretchable self-powered patchable sensor platform with ultrasensitive recognition of human activities, *ACS Nano* 9 (2015) 8801–8810.
- [6] C. Keplinger, J.Y. Sun, C.C. Foo, P. Rothemund, G.M. Whitesides, Z. Suo, Stretchable, transparent, ionic conductors, *Science* 341 (2013) 984–987.
- [7] T.Q. Trung, L.T. Duy, S. Ramasundaram, N.-E. Lee, Transparent, stretchable, and rapid-response humidity sensor for body-attachable wearable electronics, *Nano Res.* 10 (2017) 2021–2033.
- [8] X.-T. Wang, T. Ouyang, L. Wang, J.-H. Zhong, T. Ma, Z.-Q.J.A.C. Liu, Redox-inert

- Fe³⁺ Ions in octahedral sites of Co-Fe spinel oxides with enhanced oxygen catalytic activity for rechargeable zinc-air batteries, *Angew. Chem. Int. Ed. Engl.* 58 (2019) 13291–13296.
- [9] G.F. Chen, X.X. Li, L.Y. Zhang, N. Li, T.Y. Ma, Z.Q. Liu, A porous perchlorate-doped polypyrrole nanocoating on nickel nanotube arrays for stable wide-potential-window supercapacitors, *Adv. Mater.* 28 (2016) 7680–7687.
- [10] X.-X. Li, X.-T. Wang, K. Xiao, T. Ouyang, N. Li, Z.-Q.J.J.O.P.S. Liu, In situ formation of consubstantial NiCo₂S₄ nanorod arrays toward self-standing electrode for high activity supercapacitors and overall water splitting, *J. Power Sources* 402 (2018) 116–123.
- [11] K. Xiao, T.-Q. Xiao, Y. Zhang, J. Xie, M. Cao, N. Li, T. Ouyang, Z.-Q.J.C.c. Liu, In situ evolution of the active phase on stainless steel mesh toward a cost-effective bi-functional electrode for energy storage and conversion, *Chem. Commun.* 55 (2019) 2513–2516.
- [12] X.-X. Li, X.-H. Deng, Q.-J. Li, S. Huang, K. Xiao, Z.-Q. Liu, Y.J.E.A. Tong, Hierarchical double-shelled poly (3, 4-ethylenedioxythiophene) and MnO₂ decorated Ni nanotube arrays for durable and enhanced energy storage in supercapacitors, *Electrochim. Acta* 264 (2018) 46–52.
- [13] Y.-H. Liu, J.-L. Xu, S. Shen, X.-L. Cai, L.-S. Chen, S.-D. Wang, High-performance, ultra-flexible and transparent embedded metallic mesh electrodes by selective electrodeposition for all-solid-state supercapacitor applications, *J. Mater. Chem. A* 5 (2017) 9032–9041.
- [14] G.A. Snook, P. Kao, A.S. Best, Conducting-polymer-based supercapacitor devices and electrodes, *J. Power Sources* 196 (2011) 1–12.
- [15] Y. Tian, R. Xue, X. Zhou, Z. Liu, L. Huang, Double layer capacitor based on active carbon and its improved capacitive properties using redox additive electrolyte of anthraquinonedisulphonate, *Electrochim. Acta* 152 (2015) 135–139.
- [16] M. Conte, Supercapacitors technical requirements for new applications, *Fuel Cells* 10 (2010) 806–818.
- [17] L.T. Le, M.H. Ervin, H. Qiu, B.E. Fuchs, W.Y. Lee, Graphene supercapacitor electrodes fabricated by inkjet printing and thermal reduction of graphene oxide, *Electrochem. Commun.* 13 (2011) 355–358.
- [18] T. Chen, L. Dai, Carbon nanomaterials for high-performance supercapacitors, *Mater. Today* 16 (2013) 272–280.
- [19] J. Yan, Z. Fan, T. Wei, W. Qian, M. Zhang, F. Wei, Fast and reversible surface redox reaction of graphene-MnO₂ composites as supercapacitor electrodes, *Carbon* 48 (2010) 3825–3833.
- [20] H. Wang, Q. Hao, X. Yang, L. Lu, X. Wang, Graphene oxide doped polyaniline for supercapacitors, *Electrochim. Commun.* 11 (2009) 1158–1161.
- [21] Y. Xie, Y. Liu, Y. Zhao, Y.H. Tsang, S.P. Lau, H. Huang, Y. Chai, Stretchable all-solid-state supercapacitor with wavy shaped polyaniline/graphene electrode, *J. Mater. Chem. A* 2 (2014) 9142–9149.
- [22] R. Xu, A. Zverev, A. Hung, C. Shen, L. Irie, G. Ding, M. Whitmeyer, L. Ren, B. Griffin, J. Melcher, L. Zheng, X. Zang, M. Sanghadasa, L. Lin, Kirigami-inspired, highly stretchable micro-supercapacitor patches fabricated by laser conversion and cutting, *Microsyst. Nanoeng.* 4 (2018) 36.
- [23] C. Yu, C. Masarapu, J. Rong, B. Wei, H. Jiang, Stretchable supercapacitors based on buckled single-walled carbon-nanotube macrofilms, *Adv. Mater.* 21 (2009) 4793–4797.
- [24] L. Hu, M. Pasta, F. La Mantia, L. Cui, S. Jeong, H.D. Deshazer, J.W. Choi, S.M. Han, Y. Cui, Stretchable, porous, and conductive energy textiles, *Nano Lett.* 10 (2010) 708–714.
- [25] X. Li, T. Gu, B. Wei, Dynamic and galvanic stability of stretchable supercapacitors, *Nano Lett.* 12 (2012) 6366–6371.
- [26] Z. Yang, J. Deng, X. Chen, J. Ren, H. Peng, A highly stretchable, fiber-shaped supercapacitor, *Angew. Chem. Int. Ed.* 52 (2013) 13453–13457.
- [27] S. Pay, Y. Baghzouz, Effectiveness of battery-supercapacitor combination in electric vehicles, *Power Tech Conference Proceedings, 2003 IEEE Bologna*, 2003, pp. 6 pp. Vol.3.
- [28] T. Minami, Present status of transparent conducting oxide thin-film development for Indium-Tin-Oxide (ITO) substitutes, *Thin Solid Films* 516 (2008) 5822–5828.
- [29] Y.-H. Liu, J.-L. Xu, X. Gao, Y.-L. Sun, J.-J. Lv, S. Shen, L.-S. Chen, S.-D. Wang, Freestanding transparent metallic network based ultrathin, foldable and designable supercapacitors, *Energy Environ. Sci.* 10 (2017) 2534–2543.
- [30] S.W. Jin, Y.H. Lee, K.M. Yeom, J. Yun, H. Park, Y.R. Jeong, S.Y. Hong, G. Lee, S.Y. Oh, J.H. Lee, J.H. Noh, J.S. Ha, Highly durable and flexible transparent electrode for flexible optoelectronic applications, *ACS Appl. Mater. Interfaces* 10 (2018) 30706–30715.
- [31] I. Ryu, M. Yang, H. Kwon, H.K. Park, Y.R. Do, S.B. Lee, S. Yim, Coaxial RuO₂-ITO nanopillars for transparent supercapacitor application, *Langmuir* 30 (2014) 1704–1709.
- [32] P.J. King, T.M. Higgins, S. De, N. Nicolooso, J.N. Coleman, Percolation effects in supercapacitors with thin transparent carbon nanotube electrodes, *ACS Nano* 6 (2012) 1732–1741.
- [33] J.A. Fan, W.-H. Yeo, Y. Su, Y. Hattori, W. Lee, S.-Y. Jung, Y. Zhang, Z. Liu, H. Cheng, L. Falgout, M. Bajema, T. Coleman, D. Gregoire, R.J. Larsen, Y. Huang, J.A. Rogers, Fractal design concepts for stretchable electronics, *Nature Commun.* 5 (2014) 3266.
- [34] S. Xu, Y. Zhang, J. Cho, J. Lee, X. Huang, L. Jia, J.A. Fan, Y. Su, J. Su, H. Zhang, H. Cheng, B. Lu, C. Yu, C. Chuang, T.-I. Kim, T. Song, K. Shigeta, S. Kang, C. Dagdeviren, I. Petrov, P.V. Braun, Y. Huang, U. Paik, J.A. Rogers, Stretchable batteries with self-similar serpentine interconnects and integrated wireless recharging systems, *Nat. Commun.* 4 (2013) 1543.
- [35] D.J. Cohen, D. Mitra, K. Peterson, M.M. Mahabiriz, A highly elastic, capacitive strain gauge based on percolating nanotube networks, *Nano Lett.* 12 (2012) 1821–1825.
- [36] D. Lee, H.P. Hong, M.J. Lee, C.W. Park, N.K. Min, A prototype high sensitivity load cell using single walled carbon nanotube strain gauges, *Sens. Actuators A: Phys.* 180 (2012) 120–126.
- [37] M. Amjadi, K.U. Kyung, I. Park, M. Sitti, Stretchable, skin-mountable, and wearable strain sensors and their potential applications: a review, *Adv. Funct. Mater.* 26 (2016) 1678–1698.
- [38] T.Q. Trung, N.E. Lee, Flexible and stretchable physical sensor integrated platforms for wearable human-activity monitoring and personal healthcare, *Adv. Mater.* 28 (2016) 4338–4372.
- [39] Y. Cheng, R. Wang, J. Sun, L. Gao, A Stretchable and highly sensitive graphene-based fiber for sensing tensile strain bending, and torsion, *Adv. Mater.* 27 (2015) 7365–7371.
- [40] T. Yamada, Y. Hayamizu, Y. Yamamoto, Y. Yomogida, A. Izadi-Najafabadi, D.N. Futaba, K. Hata, A stretchable carbon nanotube strain sensor for human-motion detection, *Nature Nanotechnol.* 6 (2011) 296.
- [41] I. Kang, M.J. Schulz, J.H. Kim, V. Shanov, D. Shi, A carbon nanotube strain sensor for structural health monitoring, *Smart Mater. Struct.* 15 (2006) 737–748.
- [42] H. Tian, Y. Shu, Y.-L. Cui, W.-T. Mi, Y. Yang, D. Xie, T.-L. Ren, Scalable fabrication of high-performance and flexible graphene strain sensors, *Nanoscale* 6 (2014) 699–705.
- [43] X. Li, R. Zhang, W. Yu, K. Wang, J. Wei, D. Wu, A. Cao, Z. Li, Y. Cheng, Q. Zheng, R.S. Ruoff, H. Zhu, Stretchable and highly sensitive graphene-on-polymer strain sensors, *Sci. Rep.* 2 (2012) 870.
- [44] X. Yang, Z.Y. Zhou, F.Z. Zheng, M. Zhang, J. Zhang, Y.G. Yao, A high sensitivity single-walled carbon-nanotube-array-based strain sensor for weighing, *TRANSDUCERS 2009–2009 international solid-state sensors, Actuators Microsys. Conf.* (2009) 1493–1496.
- [45] X.-W. Fu, Z.-M. Liao, J.-X. Zhou, Y.-B. Zhou, H.-C. Wu, R. Zhang, G. Jing, J. Xu, X. Wu, W. Guo, D. Yu, Strain dependent resistance in chemical vapor deposition grown graphene, *Appl. Phys. Lett.* 99 (2011) 213107.
- [46] C. Yan, J. Wang, W. Kang, M. Cui, X. Wang, C.Y. Foo, K.J. Chee, P.S. Lee, Highly stretchable piezoresistive graphene-nanocellulose nanopaper for strain sensors, *Adv. Mater.* 26 (2014) 2022–2027.
- [47] Q. Fan, Z. Qin, S. Gao, Y. Wu, J. Pionteck, E. Mäder, M. Zhu, The use of a carbon nanotube layer on a polyurethane multifilament substrate for monitoring strains as large as 400%, *Carbon* 50 (2012) 4085–4092.
- [48] D.-S. Leem, A. Edwards, M. Faist, J. Nelson, D.D.C. Bradley, J.C. de Mello, Efficient organic solar cells with solution-processed silver nanowire electrodes, *Adv. Mater.* 23 (2011) 4371–4375.
- [49] L. Hu, H.S. Kim, J.-Y. Lee, P. Peumans, Y. Cui, Scalable coating and properties of transparent flexible, silver nanowire electrodes, *ACS Nano* 4 (2010) 2955–2963.
- [50] G.-W. Huang, H.-M. Xiao, S.-Y. Fu, Wearable electronics of silver-nanowire/poly(dimethylsiloxane) nanocomposite for smart clothing, *Sci. Rep.* 5 (2015) 13971.
- [51] E. Roh, B.-U. Hwang, D. Kim, B.-Y. Kim, N.-E. Lee, Stretchable, transparent, ultra-sensitive, and patchable strain sensor for human-machine interfaces comprising a nanohybrid of carbon nanotubes and conductive elastomers, *ACS Nano* 9 (2015) 6252–6261.
- [52] L.M. Zhang, Y. He, S. Cheng, H. Sheng, K. Dai, W.J. Zheng, M.X. Wang, Z.S. Chen, Y.M. Chen, Z. Suo, Self-healing, adhesive, and highly stretchable iongel as a strain sensor for extremely large deformation, *Small* 15 (2019) 1804651.
- [53] Z. Yang, Y. Pang, X.-L. Han, Y. Yang, J. Ling, M. Jian, Y. Zhang, Y. Yang, T.-L. Ren, Graphene Textile strain sensor with negative resistance variation for human motion detection, *ACS Nano* 12 (2018) 9134–9141.
- [54] P. Tamilarasan, S. Ramaprabhu, Stretchable supercapacitors based on highly stretchable ionic liquid incorporated polymer electrolyte, *Mater. Chem. Phys.* 148 (2014) 48–56.
- [55] A.M. Schilderman, S. Raeissi, C.J. Peters, Solubility of carbon dioxide in the ionic liquid 1-ethyl-3-methylimidazolium bis(trifluoromethylsulfonyl)imide, *Fluid Phase Equilibr.* 260 (2007) 19–22.
- [56] E.K. Goharshadi, Y. Ding, P. Nancarrow, Green synthesis of ZnO nanoparticles in a room-temperature ionic liquid 1-ethyl-3-methylimidazolium bis(trifluoromethylsulfonyl)imide, *J. Phys. Chem. Solids* 69 (2008) 2057–2060.
- [57] I.T. Amr, A. Al-Amer, S.T. P., M. Al-Harthi, S.A. Girei, R. Sougrat, M.A. Atieh, Effect of acid treated carbon nanotubes on mechanical, rheological and thermal properties of polystyrene nanocomposites, *Compos. Part B: Eng.* 42 (2011) 1554–1561.
- [58] H. Wang, Z. Lu, D. Qian, Y. Li, W. Zhang, Single-crystal α -MnO₂nanorods: synthesis and electrochemical properties, *Nanotechnology* 18 (2007) 115616.
- [59] P.R. Jadhav, V.V. Shinde, G.J. Navathe, M.M. Karanjkar, P.S. Patil, Manganese oxide thin films deposited by SILAR method for supercapacitor application, *AIP Conf. Proc.* 1536 (2013) 679–680.
- [60] H. Chen, X. Dong, J. Shi, J. Zhao, Z. Hua, J. Gao, M. Ruan, D. Yan, Templated synthesis of hierarchically porous manganese oxide with a crystalline nanorod framework and its high electrochemical performance, *J. Mater. Chem.* 17 (2007) 855–860.
- [61] H.-Q. Wang, J. Chen, S.-J. Hu, X.-H. Zhang, X.-P. Fan, J. Du, Y.-G. Huang, Q.-Y. Li, Direct growth of flower-like 3D MnO₂ ultrathin nanosheets on carbon paper as efficient cathode catalyst for rechargeable Li-O₂ batteries, *RSC Adv.* 5 (2015) 72495–72499.
- [62] G. Vijayakumari, N. Selvakumar, K. Jeyasubramanian, R. Mala, Investigation on the electrical properties of polymer metal nanocomposites for physiological sensing applications, *Phys. Procedia* 49 (2013) 67–78.
- [63] B.W.C. Fei, S.A. Hanifah, A. Ahmad, N.H. Hassan, Polymer electrolyte based on crosslinked poly(glycidyl methacrylate) and 1-butyl-3-methylimidazolium bis(trifluoromethylsulfonyl)imide, *AIP Conf. Proc.* 1678 (2015) 050009.
- [64] Z. Wang, Y. Han, Y. Zeng, Y. Qie, Y. Wang, D. Zheng, X. Lu, Y. Tong, Activated carbon fiber paper with exceptional capacitive performance as a robust electrode for supercapacitors, *J. Mater. Chem. A* 4 (2016) 5828–5833.
- [65] M.F. El-Kady, R.B. Kaner, Scalable fabrication of high-power graphene micro-

- supercapacitors for flexible and on-chip energy storage, *Nature Commun.* 4 (2013) 1475.
- [66] H. Yu, J. Wu, L. Fan, K. Xu, X. Zhong, Y. Lin, J. Lin, Improvement of the performance for quasi-solid-state supercapacitor by using PVA-KOH-KI polymer gel electrolyte, *Electrochim. Acta* 56 (2011) 6881–6886.
- [67] Y. Zhu, S. Murali, M.D. Stoller, K.J. Ganesh, W. Cai, P.J. Ferreira, A. Pirkle, R.M. Wallace, K.A. Cychosz, M. Thommes, D. Su, E.A. Stach, R.S. Ruoff, Carbon-based supercapacitors produced by activation of graphene, *Science* 332 (2011) 1537.
- [68] Y. Shi, L. Pan, B. Liu, Y. Wang, Y. Cui, Z. Bao, G. Yu, Nanostructured conductive polypyrrole hydrogels as high-performance, flexible supercapacitor electrodes, *J. Mater. Chem. A* 2 (2014) 6086–6091.
- [69] J. Yun, Y. Lim, H. Lee, G. Lee, H. Park, S.Y. Hong, S.W. Jin, Y.H. Lee, S.-S. Lee, J.S. Ha, A patterned graphene/ZnO UV sensor driven by integrated asymmetric micro-supercapacitors on a liquid metal patterned foldable paper, *Advanced Functional Materials* 27 (2017) 1700135.
- [70] F.O. Agyemang, G.M. Tomboc, S. Kwofie, H. Kim, Electrospun carbon nanofiber-carbon nanotubes coated polyaniline composites with improved electrochemical properties for supercapacitors, *Electrochim. Acta* 259 (2018) 1110–1119.
- [71] H. Yang, N. Wang, Q. Xu, Z. Chen, Y. Ren, J.M. Razal, J. Chen, Fabrication of graphene foam supported carbon nanotube/polyaniline hybrids for high-performance supercapacitor applications, *2D, Materials* 1 (2014) 034002.
- [72] P. Li, Y. Yang, E. Shi, Q. Shen, Y. Shang, S. Wu, J. Wei, K. Wang, H. Zhu, Q. Yuan, A. Cao, D. Wu, Core-double-shell, carbon nanotube@polypyrrole@MnO₂ sponge as freestanding, compressible supercapacitor electrode, *ACS Appl. Mater. Interfaces* 6 (2014) 5228–5234.
- [73] A. Lewandowski, A. Olejniczak, M. Galinski, I. Stepniaik, Performance of carbon–carbon supercapacitors based on organic, aqueous and ionic liquid electrolytes, *J. Power Sources* 195 (2010) 5814–5819.